THE INELASTIC CONTRIBUTION TO HIGH RESOLUTION IMAGES OF DEFECTS

O.L. Krivanek[1] , C.C. Ahn[2] and G.J. Wood[3]

Center for Solid State Science and the Department of Physics, Arizona State University, Tempe, AZ 85287, USA

1 now at Gatan R&D, 6678 Owens Drive, Pleasanton, CA 94588, USA

2 now at Keck Laboratory of Engineering Materials, California Institute of Technology, Pasadena, CA 91125, USA

3 now at School of Physics, University of Melbourne, Parkville, Victoria 3052, Australia

The importance of the contribution due to inelastically scattered electrons to unfiltered HREM images is examined, with emphasis on imaging of defects in semiconductors. Whenever the low energy loss spectrum contains sharp peaks, the contribution is not featureless. At specimen thickness of a few tens of nm, it may change the image appearance in a major way. The strongest effect occurs in high resolution, medium voltage (200 to 500 kV) electron microscope images of defects at focus values minimizing the contrast of the elastic image in low Z materials such as Al and Si. In higher Z materials or those with no sharp "plasmons", the contribution is small.

submitted to Ultramicroscopy

1. Introduction

Inelastic scattering of medium energy electrons by light elements is of similar strength as elastic scattering [1] yet its effect on high resolution electron microscope (HREM) images of defects is typically not taken into account. In the few cases in which it is considered, it is usually modelled with an absorption-like term [2], implying that the inelastic scattering contribution is featureless. In reality, however, the combination of inelastic and elastic scattering may result in sharp image features dissimilar to any features produced by purely elastic scattering, and these may significantly alter the appearance of a high resolution image.

The fact that the inelastic contribution can produce strong contrast is best documented by energy-filtered images of lattice fringes in dysprosium oxide, which have been produced with a scanning transmission electron microscope (STEM) using electrons that have lost 16 and 37 eV energy [3]. Similarly, lattice images of crystalline Si have been produced using plasmon-loss electrons in a conventional transmission electron microscope (CTEM) equipped with an imaging filter [4, 5]. Electrons scattered inelastically have also been shown to contribute distinct features to the images of amorphous materials [6]. The inelastic contribution may modify the image of both the crystalline lattice, and of lattice defects. In the latter case, the modification may easily lead to an erroneus determination of the defect structure, which makes the inelastic contribution to the images of defects especially important.

The safest way of dealing with the inelastic contribution is to exclude it by using an energy-filtering microscope. However, most high resolution electron microscopes in use today have no means for energy selection. One approach suitable for interpreting images produced by such microscopes is to include the inelastic contribution within the framework of a computer program normally used for calculating images due to purely elastic scattering. Programs using either the

multislice [7] or the Bloch wave [8] formulations can be adapted to this purpose. Another possibility would be to use a formulation of the image-formation process which takes account of inelastic scattering from the very beginning. However, formulations of this type are presently restricted to very thin specimens, and have only been used to simulate images of single atoms, and of abrupt edges of jellium [9,10].

An approach suited to more practical applications has been independently developed by us in the present paper as originally submitted, and by Boothroyd and Stobbs, who evaluated the importance of the inelastic contribution to high resolution images of a (Al, Ga)As/GaAs interface [11,12]. Here we summarize the main points of the approach, present experimental data documenting the strength of the inelastic channel, show calculated images of a defect in a silicon crystal which illustrate the importance of the inelastic contribution, and discuss the conditions under which the inelastic contribution to the images of defects will be significant.

2. Theory

Two types of inelastic scattering events are relevant to unfiltered HREM images: phonon scattering, which deflects the electrons by angles comparable to Bragg scattering and results in energy losses of a few meV, and plasmon (and other low loss) scattering, which is typically much smaller in angle and about 10 to 40 eV in energy. Both types of events deplete the elastic wavefield, which leads to an overall loss of contrast. The phonon scattering may produce weak additional high resolution image contrast, but such contrast has not been observed experimentally and its existence is even doubtful theoretically [13].

Because the plasmon, interband and intraband scattering is mostly small in angle and thus delocalized in real space, it cannot by itself produce any atomic-scale image features. However,

the low-angle inelastic scattering event may be followed (or preceded) by high-angle elastic scattering, and the double scattering may give rise to sharp image features. Since the two scattering events are independent, the simplest way to consider the effect of the inelastic scattering on unfiltered images is to model the image formation as if due to an incident beam with an energy distribution identical to the spectrum of energy losses from the area of interest. The angular spread of the beam is determined as the convolution product of the angular spread of the incident beam with the angular spread due to the inelastic scattering, and is different for each energy. The total image is then worked out by calculating partial images for all the different energies, and adding them up incoherently with weights determined by the intensity distribution of the energy loss spectrum. Because the elastic scattering is essentially the same for all the low energy losses, only the imaging part of the image calculation needs to be performed for each partial image, and the order in which the elastic and inelastic scattering events occur does not need to be considered.

The simplest situation in which the inelastic scattering can be expected to give a major image contribution arises when a sharp and strong plasmon is present in the energy loss spectrum. In this case the total image can be considered as the sum of two partial images, the purely elastic one $I_e(r)$, which is formed with an incident beam of primary energy E_o, energy spread ΔE_o, and angular spread α_o, and an inelastic-elastic one $I_i(r)$, which is similar to an elastic image formed with a beam of primary energy $E_o - E_p$, where E_p is the plasmon energy, energy spread of

$$\Delta E_i = (\Delta E_e^2 + \Delta E_p^2)^{1/2} , \qquad (1a)$$

where ΔE_p is the plasmon energy width, and angular spread of

$$\alpha_i = [\alpha_e^2 + (E_p/2E_o)^2]^{1/2} . \qquad (1b)$$

The two images are then added incoherently to give the total image

$$I(r) = \frac{1}{1+t/\lambda_p} I_e(r) + \frac{t/\lambda_p}{1+t/\lambda_p} I_i(r) , \qquad (2)$$

where t is the specimen thickness and λ_p the mean-free path of the plasmon loss.

In practice the inelastic image will resemble an elastic one obtained at a slight overfocus (stronger lens) relative to the elastic one, but it will be more strongly attenuated by the larger energy and angular spread of the inelastic "incident beam". The focus difference will be simply

$$\Delta Z = (E_p/E_o)\ C_c , \qquad (3)$$

where C_c is the coefficient of chromatic aberration of the microscope objective lens. For a 200 kV, C_c =1.2 mm electron microscope, and E_p =16.5 eV (E_p in Si), the defocus difference is 99 nm. This is large enough to produce an inelastic image substantially different from the elastic image, yet not as large as to ensure that any contrast in the inelastic image will be destroyed by incoherence effects.

3. Measurement of the mean free path of the inelastic scattering

Experimental data on inelastic mean free paths is available for only a few materials [1,14]. It is therefore important to be able to determine the mean free path experimentally, preferably in the same microscope as used for the high resolution imaging.

The collection of the necessary energy loss spectra presents no problems if the microscope is equipped with an energy loss spectrometer, but the determination of the specimen thickness requires some attention. Sample areas suitable for EELS are generally very thin (< 50 nm),

whereas thickness determination by convergent beam diffraction [15] works best in specimens of medium thickness (100 to 200 nm). Further, HREM samples prepared by crushing or ion beam milling tend to be in the form of steep wedges, and the rapid change in thickness presents another difficulty.

The approach adopted here was to determine the sample thickness from the extinctions of the main beam (thickness fringes) in an [011] zone axis - oriented specimen, whose dependence on thickness was determined using a modified multislice program. In addition, we checked that the (111), (200) and (220)-type lattice fringes visible in the image exhibited the predicted behavior as a function of thickness [16,17]. We then collected spectra from the same areas with a magnetic sector spectrometer (Gatan 607) mounted below the HREM column (JEM 200CX). The images and the spectra were both acquired at 850 000x direct magnification on the microscope viewing screen.

The entrance aperture into the spectrometer was 3 mm in diameter, and it was situated just below the microscope camera. Its position relative to a micrograph could be determined to within about 0.5 mm accuracy by positioning the microscope pointer so that its tip shadowed the aperture slightly. Thus we were effectively acquiring spectra from specimen areas of 3.5 nm diameter at a positioning precision of about 0.6 nm. For the small energy losses ($\leq$ 30 eV) due to electrons scattered by small angles, which are of principal interest in this study, the contribution of inelastic electrons originating more than about 1 nm outside the selected area (due to the defocussing of the inelastic image relative to the focussed elastic one) was minimal.

Figs. 1, 2 and 3 illustrate how the mean free path determination worked out in practice. Fig. 1 shows a high resolution image of [011] GaAs recorded at 200 kV, with the EELS aperture outlined by the dashed circle. Fig. 2 shows an energy loss spectrum acquired from the outlined area in 20 secs immediately after recording the micrograph. A second micrograph was recorded immediately

after the spectrum to check that no drift occurred during the EELS acquisition. The spectrum was subsequently analysed to determine the ratio between the elastic intensity I_e and the first plasmon intensity I_i. The thickness of the specimen at the location studied by EELS was determined from the position of the EELS aperture relative to the thickness fringes whose absolute thickness could be determined by multislice calculations as described above. In GaAs at 200 keV, the first three dark thickness fringes occur at thicknesses of 6.6, 20.4, and 33.1 nm (Fig. 3). Subsequent fringes are less pronounced, as observed in the image, and predicted by the calculation.

Micrograph-spectrum-micrograph data sets were acquired at various distances from the specimen edge in both GaAs (011) and Si (011), and the result for each material plotted out as graphs of I_i / I_e vs. specimen thickness. Since the probability of exciting the first plasmon and the probability of there being no inelastic scattering with an energy of greater than about 1 eV go as, respectively:

$$P(1) = t/\lambda\, e^{-t/\lambda_i} , \qquad (4a)$$

where λ_i is the mean free path for plasmon scattering, and

$$P(0) = e^{-t/\lambda_i} , \qquad (4b)$$

it follows that

$$I_i / I_e = P(1) / P(0) = t/\lambda_i . \qquad (5)$$

A graph of I_i / I_e as a function of t should therefore yield a straight line passing through the origin, with a slope of $1/\lambda_i$. The plots for both GaAs and Si did yield straight lines, but neither line passed through the origin, as shown in Fig. 4 for Si. The reason for this is almost certainly the amorphous Si and C layer covering the crystalline foil, since material in this layer contributes to the inelastic scattering, but does not affect the thickness fringes. If the layer were uniform in thickness, the

line would be shifted upwards and its intercept with the abscissa would give minus two times the layer thickness. This is precisely what happens in Fig. 4. The intercept at -8 nm indicates an amorphous layer thickness of 4 nm. This is a reasonable result for a sample which had been ion milled, and is in good agreement with the thickness of the amorphous layer visible at the specimen edge in Fig. 1.

The graph in Fig. 4 yielded $\lambda_i = 150 \pm 10$ nm for Si at 200 keV, and a similar one for GaAs gave $\lambda_i = 300 \pm 30$ nm. Since the elastic scattering is about twice weaker in Si at a given small thickness than in GaAS, and the Si plasmon is quite narrow (Fig. 5), the rest of this paper concentrates on Si as an example of a material in which the inelastic image contribution is likely to have a real practical importance.

4. Image computations

The effect of the inelastic image contribution will be particularly important in the case of defects, where it may lead to an erroneous interpretation of the core structure. We have therefore evaluated the importance of the inelastic contribution for a defect whose core structure has been determined by HREM: the $\Sigma = 9$ (38.94° tilt) grain boundary of the diamond-cubic lattice. The boundary structure was originally determined for Ge [18,19], and total energy calculations have since confirmed that it is a stable configuration in Si as well [20].

An artificial periodicity was imposed on the model by including two boundaries of opposite tilt in the same unit cell, and matching the atomic structure around the unit cell edges (Fig. 6). Strain at the boundaries was relaxed by iteratively moving each atom in a direction determined from the gradient of the local Keating potential which takes account of the force on an atom due to first and second nearest neighbour atoms [21]. This procedure enabled us to enter the initial atomic

positions based on a schematic model of the boundary, with individual atomic positions in error by as much as 0.07 nm. After 300 complete passes of the relaxation routine the atomic displacements per pass were less than 10^{-5} nm, and all atomic bond lengths were accurate to better than 10^{-3} nm.

The calculated images of the boundary model viewed in the [011] direction are shown in Fig. 7. The specimen thickness was 40 Å. A standard multislice program was used, and the images were computed from the wavefunction at exit surface. Angular illumination spreads were taken into account by incoherent summing of computed images over a range of beam tilts. For the crystal thickness considered, it was not necessary to consider the beam tilts in the multislice step. The effect of energy spread was included by taking Gaussian-weighed incoherent sums of images computed for the various appropriate defocus values. Separate images were computed for the elastic and inelastic contributions according to equations (1) and (3), weighed as described in equation (2), and then added incoherently to give the total image. The imaging parameters were: E_o = 200 keV, $C_s = C_c$ = 1.2 mm, elastic peak energy spread (full-width at half-maximum) ΔE = 2 eV, inelastic peak energy spread ΔE_p = 4.5 eV, half-width of angular illumination spread = 0.8 mrad, plasmon mean-free path λ = 150 nm, plasmon energy E_p = 16.5 eV. The effective defocus difference between the elastic and inelastic images was $\Delta Z = C_c E_p / E_o$ = 99 nm, and the ratio in which the intensities of the two images were added was I_i / I_e = 0.27.

The images show that close to the optimum elastic defocus (about 60 nm) the contribution of the inelastic image to the total image is negligible for the microscope parameters chosen. At higher underfocus values, however, the inelastic contribution becomes more important. This is because as the underfocus of the elastic image increases, its contrast becomes attenuated by spatial incoherence effects [22], while at the same time the inelastic image approaches the optimum defocus, and its contrast therefore becomes stronger. If the defocus value is such that the elastic image is at a contrast minimum while the contrast in the inelastic image is at maximum, the inelastic

contribution will be especially significant. The presence of a contamination layer, which increases the strength of the inelastic scattering, will make the effect important also in specimen areas in which the crystalline layer is thin.

In specimens whose thickness (including an amorphous contamination layer) is less than about 20 nm, and in high Z materials, the effect will be weaker. This is likely to make it unobservable in the majority of normal HREM images, though it may be quite significant in center-stop bright field and dark-field images, as shown by Boothroyd and Stobbs [11,12].

5. Discussion and conclusions

The inelastic image contribution will have an important effect on the image contrast if:

1) the specimen thickness (including the amorphous contamination layer) is at least 0.1 times the plasmon mean free path,

2) the plasmon is sufficiently narrow and the microscope chromatic aberration coefficient sufficiently low so that the effective spread of focus of the inelastic image does not completely attenuate its contrast, and

3) the image is recorded at an underfocus of a few tens of nm with respect to Scherzer defocus.

The strongest effect will be observed at a defocus setting which minimizes the contrast of the elastic image while simultaneously maximizing the inelastic image contrast.

In most materials the width of the low loss scattering distribution is larger than 10 eV [23], as shown for $Ti_2Nb_{10}O_{29}$ (an important HREM test specimen) in Fig. 8. This large width will result in images of many different effective defoci being added in a TEM with no energy filtering, and it will effectively destroy the contrast in the inelastic image contribution. However, in some specific cases the inelastic contribution may be quite important. An example from the literature where the inelastic contribution may have mattered is the study by D'Anterroches and Bourret of the $\Sigma = 9$ boundary in Ge [14], which reported good match between experimental and calculated images close to Scherzer defocus, and disagreement at higher underfocus. As shown above, the strength of the inelastic image contribution is especially important at high underfocus, making it likely that ignoring the contribution was the source of the disagreement.

Interestingly, the inelastic contribution will be more important for microscopes with smaller aberration coefficients. This can be illustrated by considering a 200 kV microscope with C_c of 0.6 mm, a figure which is probably technologically feasible. The inelastic image overfocus relative to the elastic image at 200 kV primary voltage will then be only 50 nm, and the image will therefore be only weakly attenuated at optimum elastic defocus. The contrast reversal of the linear image of (111) planes in [011] Si occurs at 40 nm intervals at 200 kV primary voltage, so the inelastic contribution will produce contrast mostly opposite to the elastic one, and at defocus values where the elastic image is weak, it may dominate the image. At higher primary voltages the defocus difference between the elastic and inelastic image will become even smaller. However, because the plasmon mean free path increases at higher voltages, the importance of the effect will decrease markedly for microscopes of primary voltage higher than 500 kV.

In summary, the inelastic contribution to normal HREM images of defects can be easily modelled using a modified multislice program. It is especially important for microscopes of 200 to 500 kV voltage, and low Z materials with sharp plasmons, such as Si, Al, B, and C, and probably also Ge, GaAs and other III-V compounds. In most other materials, such as those which do not posses

REFERENCES

[1] L. Reimer, Transmission Electron Microscopy (Springer-Verlag, Berlin), (1984).

[2] P. Pirouz, Optik 54 (1979) 69.

[3] A.J. Craven and C. Colliex, Proc. 35-th EMSA Meet. (1977), G.W. Bailey, Ed. (Claitor's Publishing, Baton Rouge) p. 242.

[4] N. Ajika, H. Hashimoto, H. Endoh, K. Yamaguchi, M. Tomita and R.F. Egerton, J. Electron Microsc. **32** (1983) 250.

[5] O.L. Krivanek and C.C. Ahn, Proceedings 11-th Int. E.M. Congress, Eds T. Imura, S. Maruse and T. Suzuki (Japanese Society of Electron Microscopy, Tokyo, 1986) vol. 1, 519.

[6] J.R. Parsons and C.W. Hoelke, Phil. Mag. 30 (1974) 135.

[7] J.M. Cowley, Diffraction Physics, (North-Holland Publ. Co., Amsterdam) 1981.

[8] P. Stadelmann, Ultramicroscopy **21** (1987) 131

[9] H. Kohl Ultramicroscopy **11** (1983) 53.

[10] H. Kohl and H. Rose, Advances in Electronics and Electron Physics **65** (1985) 173.

[11] C.B. Boothroyd and W.M. Stobbs, Ultramicroscopy **26** (1988) 361.

[12] C.B. Boothroyd and W.M. Stobbs, Ultramicroscopy **31** (1989) 259.

[13] J.C.H. Spence *in:* High Resolution Transmission Electron Microscopy, Eds P.R. Buseck, J.M. Cowley, and L. Eyring (Oxford University press, New York and oxford, 1988) p. 129.

[14] H. Raether, Excitation of Plasmons and Interband Transitions by Electrons (Springer-Verlag, Berlin) 1980.

[15] P.M. Kelly, A. Jostons, R.G. Blake and J.G. Napier Phys. Stat. Sol. **a31** (1975) 771.

[16] J. Desseaux, A. Renault, and A. Bourret, Phil. Mag. **35** (1977) 357.

[17] P. Rez and O.L. Krivanek, Proceedings 9-th Int. Congr. EM (Toronto), 1, p. 288 (1978).

[18] O.L. Krivanek, S. Isoda and K. Kobayashi, Phil. Mag. **36** (1977) 331.

[19] C. D'Anterroches and A. Bourret, Phil. Mag. **A49** (1984) 783.

[20] R.E. Thomson and D.J. Chadi, Phys. Rev. **B29** (1984) p. 889.

[21] M.G. Duffy, P.S. Boudreaux and D.E. Polk, J. Non-Cryst. Solids **15** (1974) 435.

[22] J. Frank, Optik **38** (1973) 519.

[23] C.C. Ahn and O.L. Krivanek, "EELS Atlas" (published by ASU HREM Facility and Gatan), 1983.

FIGURE CAPTIONS

Fig. 1. A high resolution image of [011] GaAs recorded at 200 keV.

Fig. 2. Energy loss spectrum collected from an area corresponding to the dashed circle in Fig. 1. Collection angle ~100 mrad.

Fig. 3. Variation of the unscattered beam intensity I_o as a function of specimen thickness in [011] oriented GaAs at 200 keV.

Fig. 4. Experimentally measured value of I_i / I_e vs. thickness in Si at 200 keV. The straight line corresponds to a mean free path of 150 nm and an amorphous Si surface layer of 4 nm thickness.

Fig. 5. Energy loss spectrum from [011] Si 41 nm thick. Primary energy 200 keV.

Fig. 6. Model of the $\Sigma = 9$ grain boundary. The unit cell (dimension 1.15 nm x 3.25 nm x .38 nm) is indicated by white lines. It contains 72 atoms and is perfectly periodic in three dimensions. The two grain boundaries are indicated by arrows.

Fig. 7. Calculated first plasmon, elastic and total images of the $\Sigma = 9$ grain boundary in Si. Primary energy 200 keV, specimen thickness 40 nm. Defocus values indicated. Only the bottom half of the unit cell is shown. Each image field size is 3.69 nm x 1.96 nm.

Fig. 8. Low loss spectrum of $Ti_2Nb_{10}O_{29}$. Primary energy 200 keV, collection angle about 100 mrad.

Fig. 1

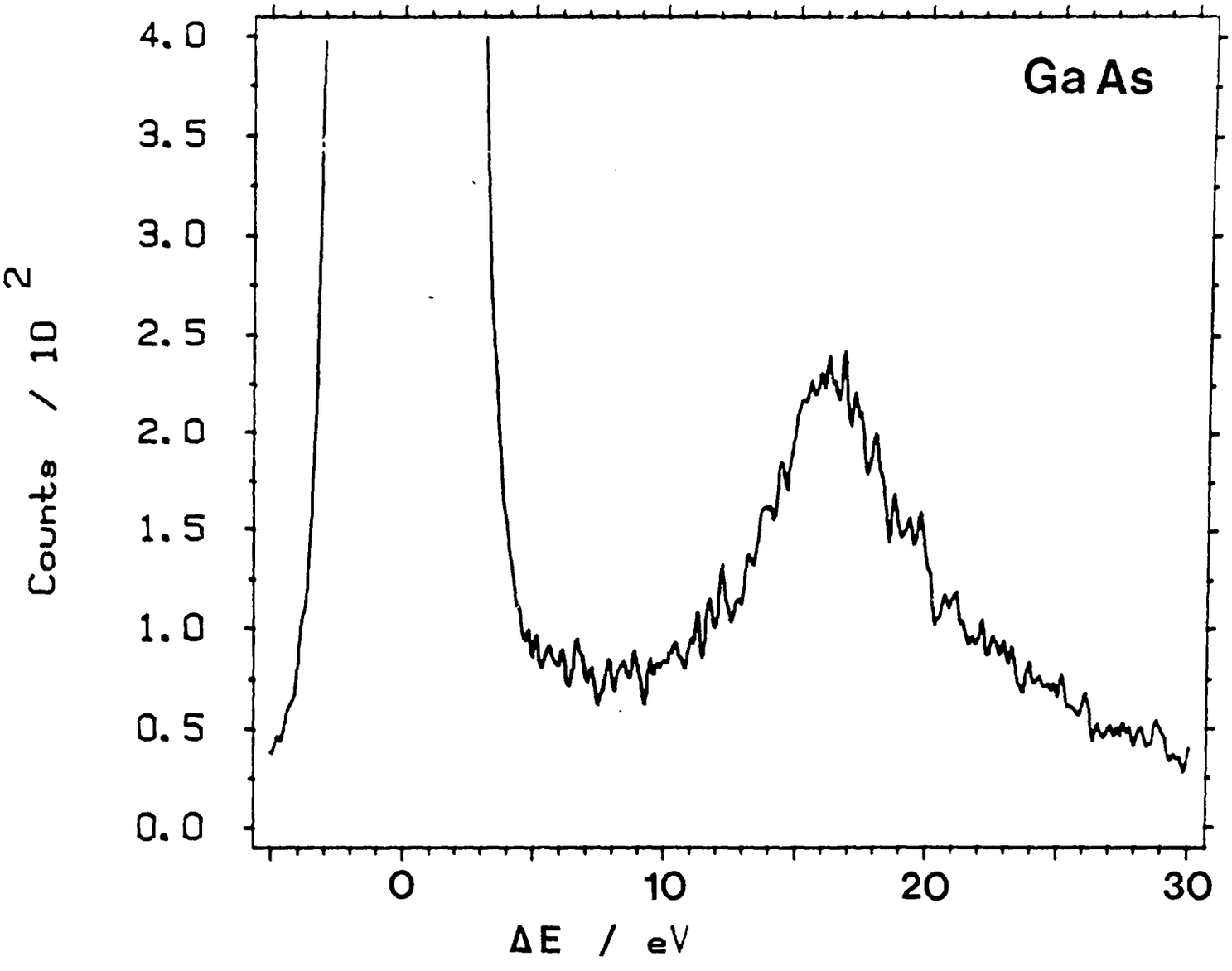

Fig. 2

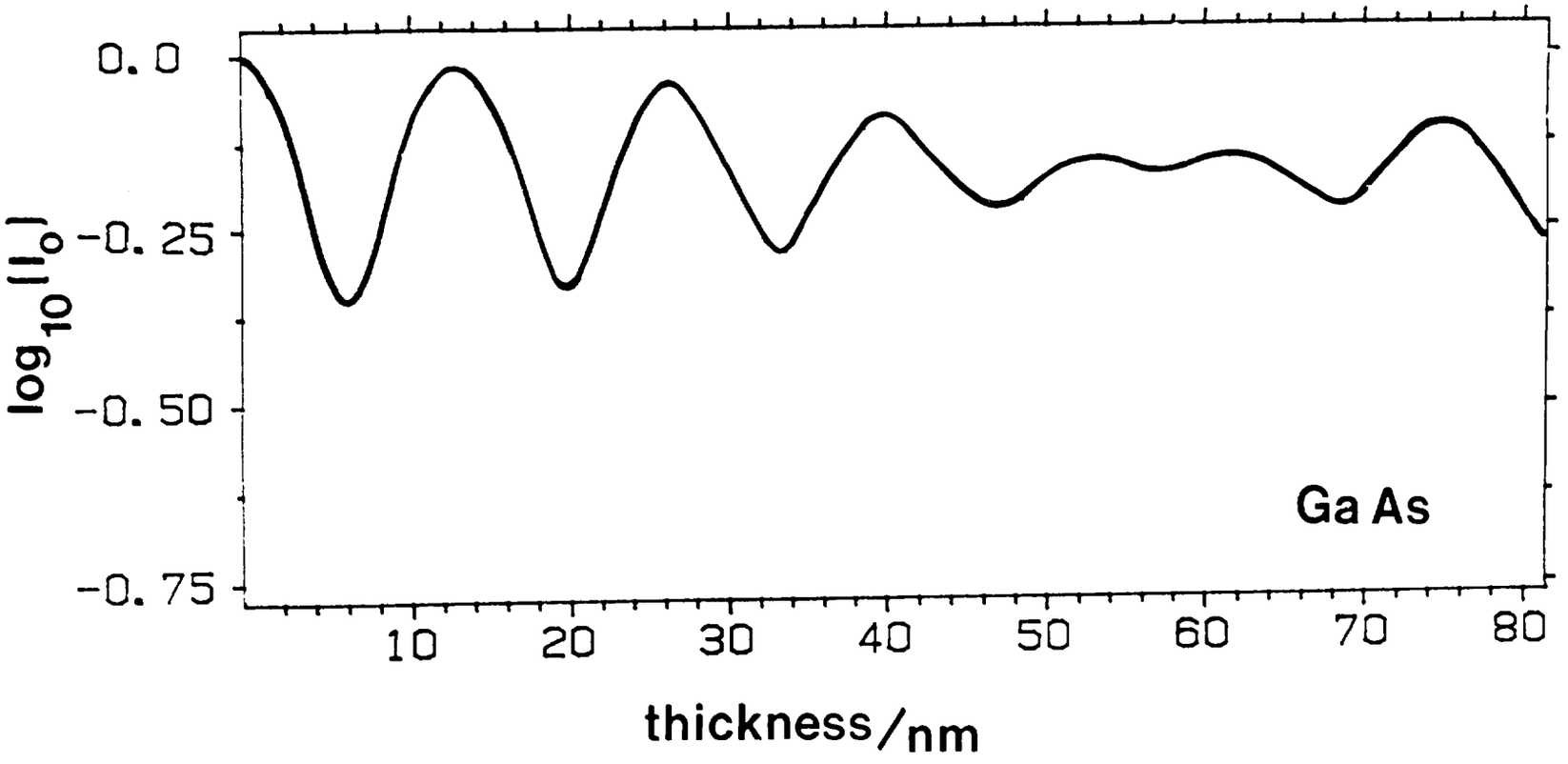

Fig. 3

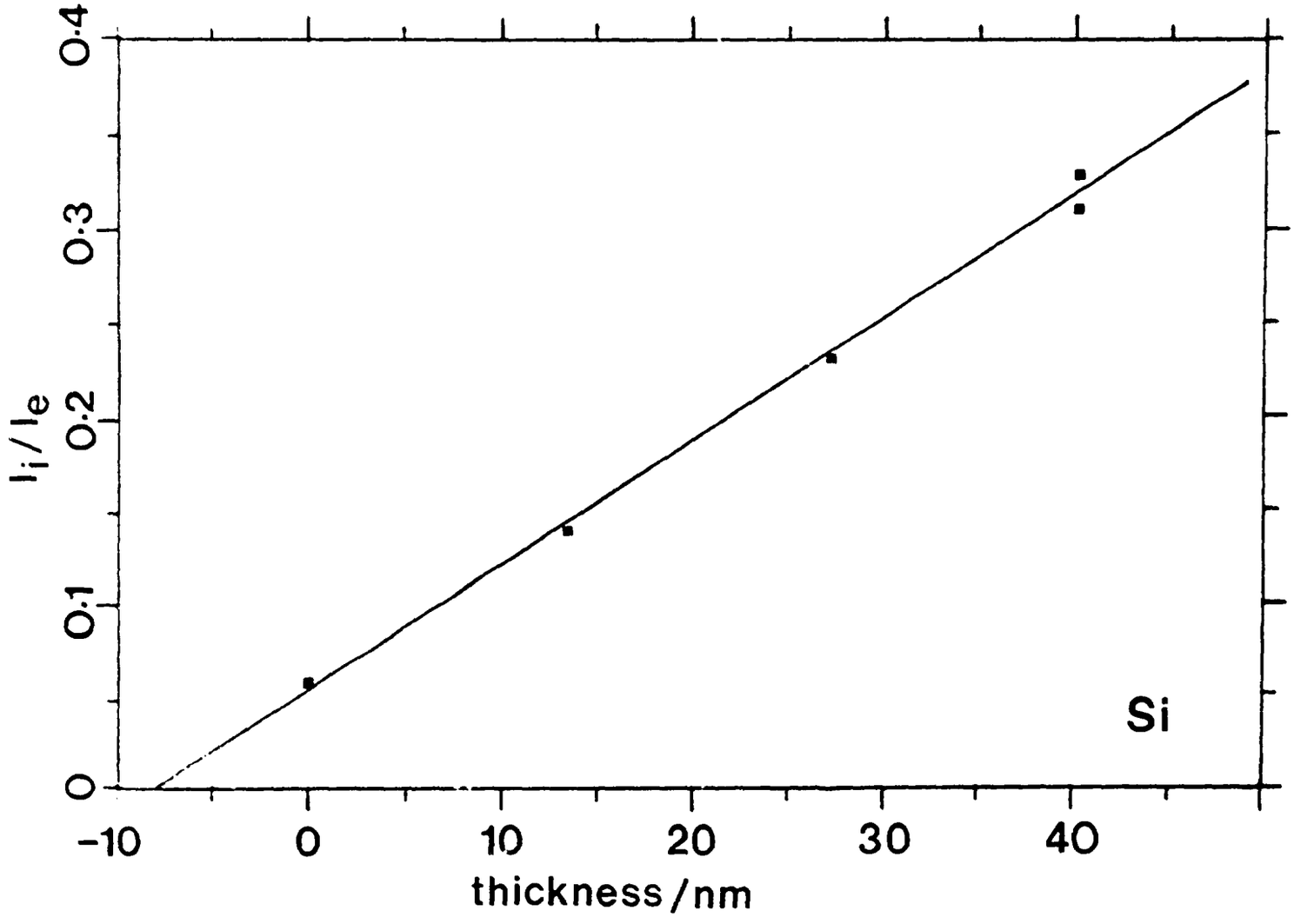

Fig. 4

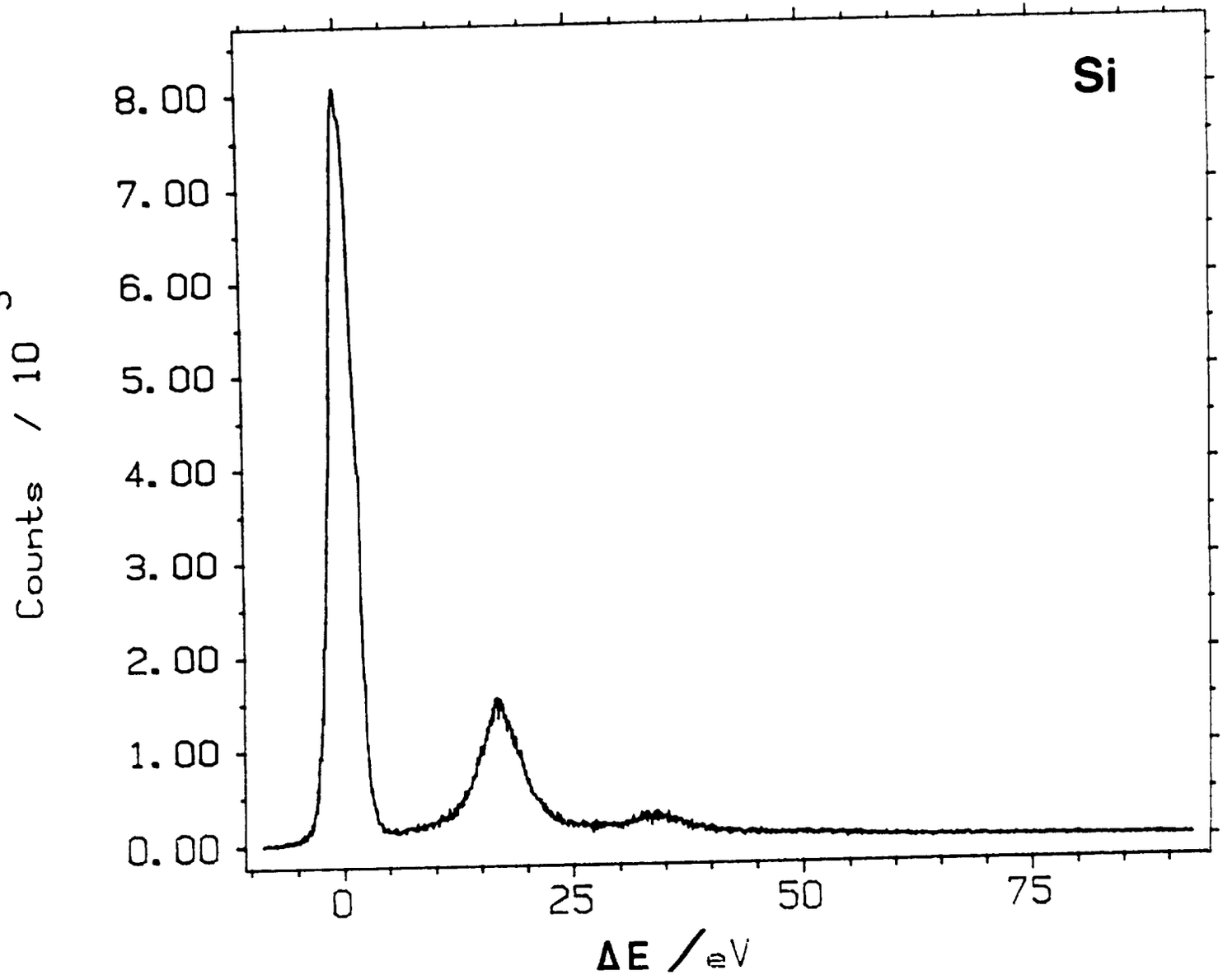

Fig. 5

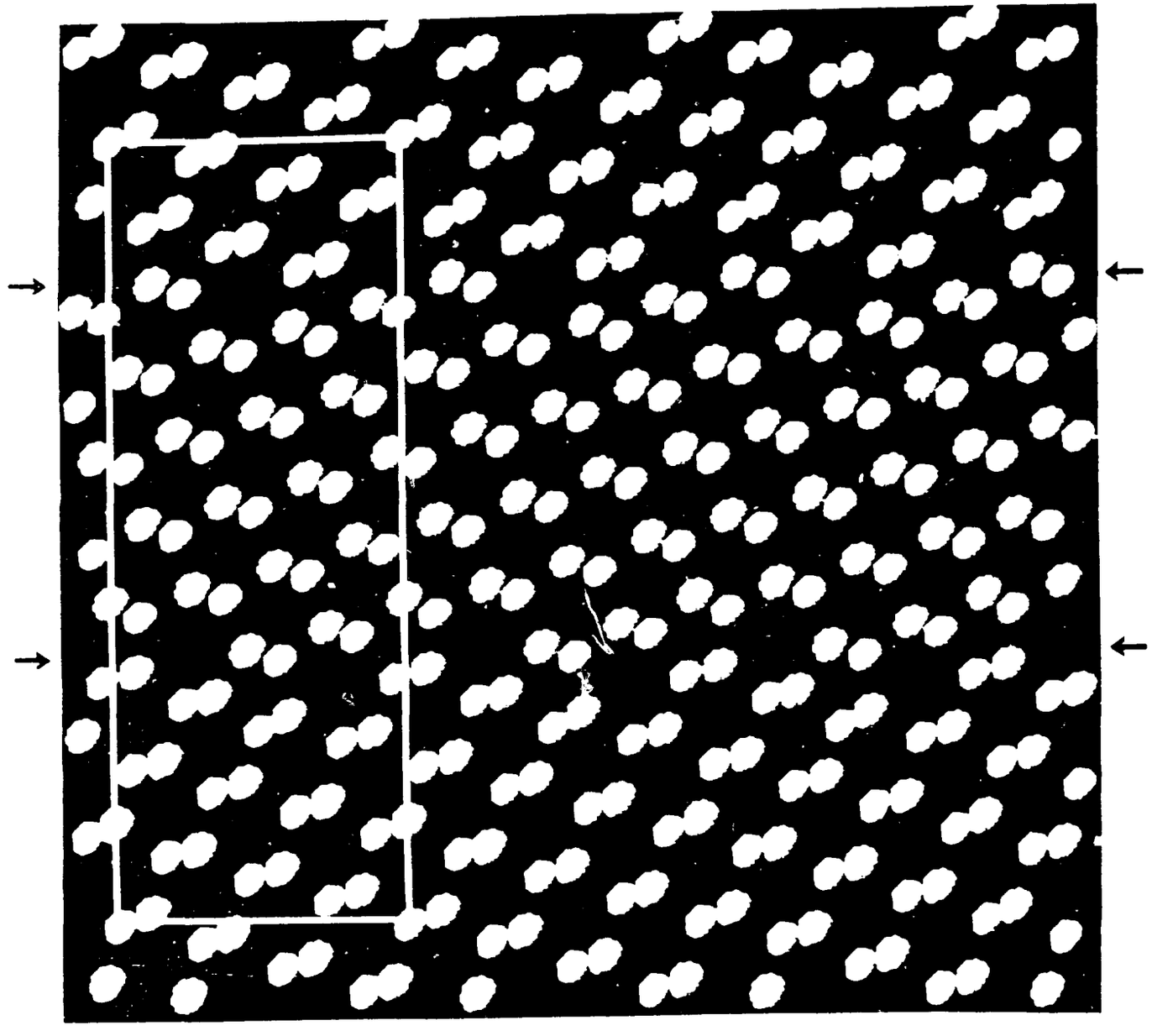

Fig.6

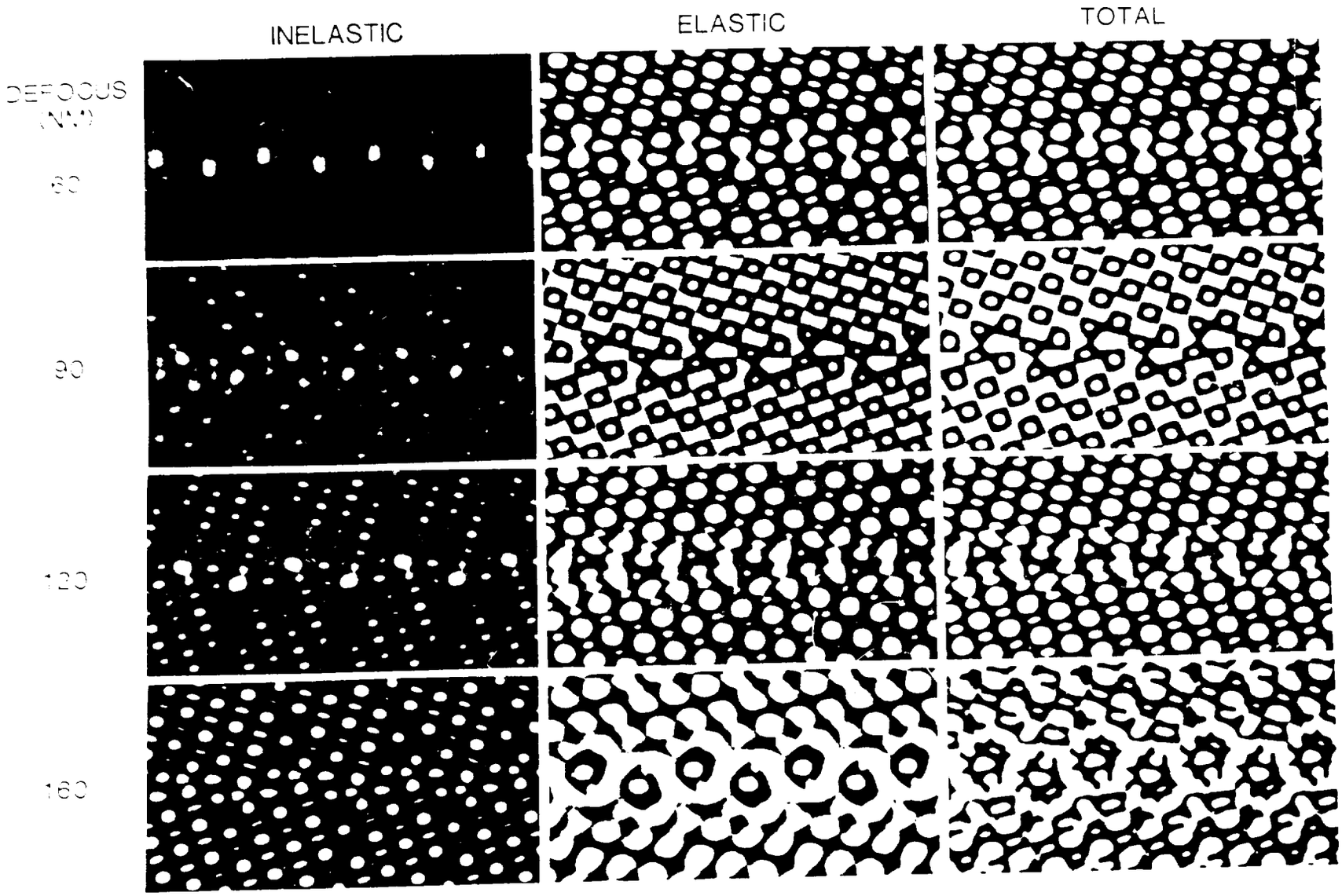

Fig. 7

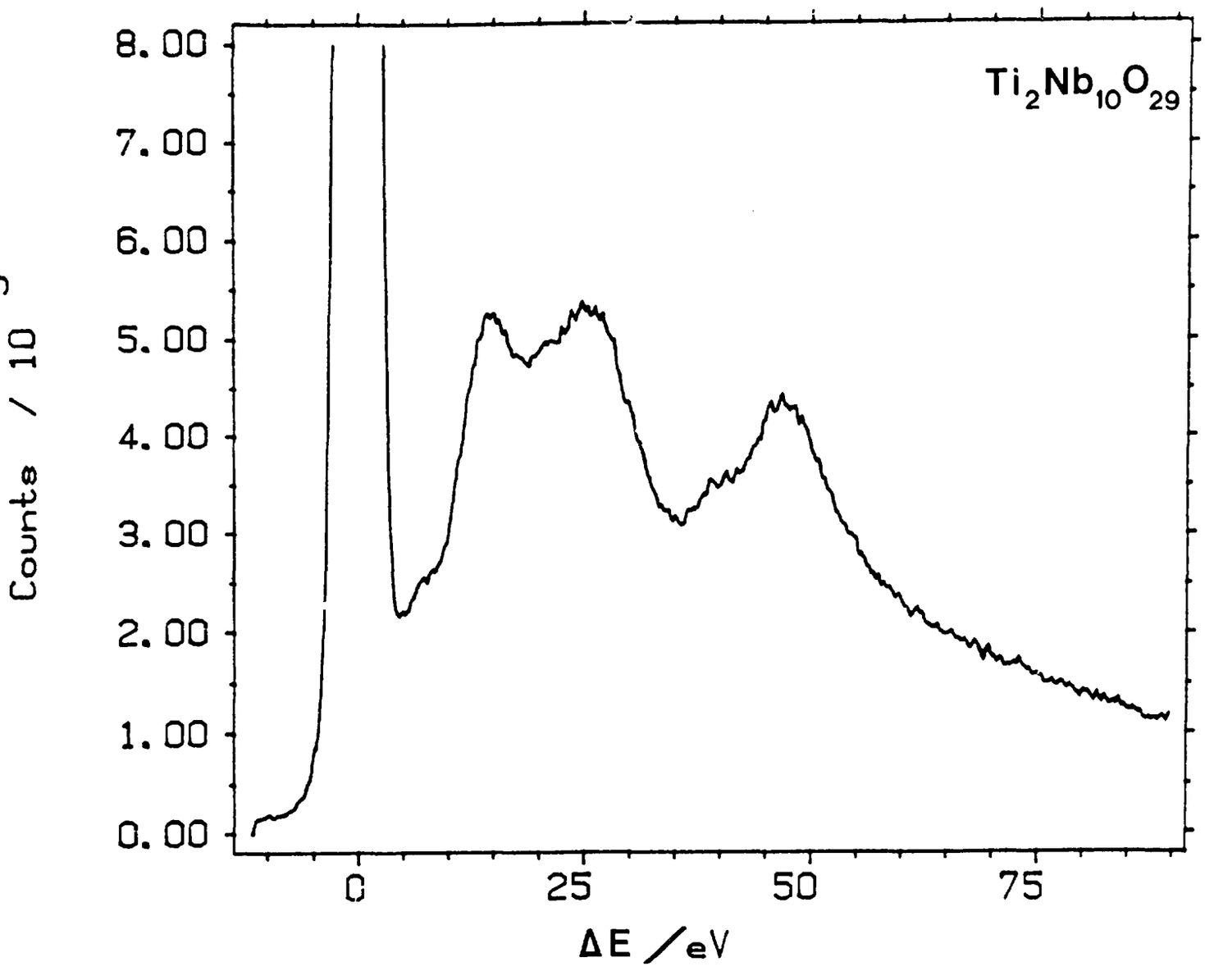
$Ti_2Nb_{10}O_{29}$
8.00
7.00
6.00
5.00
4.00
3.00
2.00
1.00
0.00
Counts / 10^3
0
25
50
75
ΔE / eV

Fig.8